ARTICLES

Rayleigh and Raman Scattering from Individual Carbon Nanotube Bundles

Zhonghua Yu and Louis Brus*

Department of Chemistry, Columbia University, New York, New York 10027

Received: August 25, 2000; In Final Form: November 21, 2000

Rayleigh scattering spectra and Raman spectra from single bundles of aligned single-wall carbon nanotubes (SWNTs) have been obtained with dark field optical microscopy and Raman microscopy. Rayleigh scattering spectrum reveals resonance peaks due to the optically allowed interband transitions in SWNTs. The intensity of the resonance peaks was found to depend strongly on the incident light polarization. These resonance peaks are completely suppressed when the incident light polarization is perpendicular to the nanotube axis, suggesting that the interband transition dipole in SWNTs is orientated parallel to the tube axis. Polarized Raman measurements on aligned nanotubes in a single bundle show that the Raman scattering is polarized along the nanotube axis direction, and Raman scattering signal is strongest when the incident laser is polarized parallel to the tube axis. All strong Raman active modes behave as A_{1g}. Tangential carbon stretching mode Raman scattering from semiconducting tubes shows very little change from bundle to bundle, while that from metallic SWNTs exhibits large variations. The broadened metallic Raman scattering at 1550 cm^{-1} can be well fitted by a Fano line shape function. This broadened Raman scattering depends sensitively on sample processing conditions. Charge transfer due to chemical doping is proposed to explain the change in Raman scattering from oxidized metallic tubes.

Introduction

Since their discovery in 1993,[1,2] single-wall carbon nanotubes (SWNTs) have been the focus of intense interest.[3,4] SWNTs exhibit unique properties and may find wide applications in nanoscale science and technology. For example, a SWNT can be either metallic or semiconducting, depending on its diameter and chirality.[3,5] Thus SWNTs are regarded as potential molecular quantum wires. Single electron transistors employing metallic nanotubes[6,7] and field-effect transistors consisting of semiconducting nanotubes[8] have been experimentally demonstrated. Recently, carbon nanotube junctions[9] were found to behave like a rectifying diode. Carbon nanotubes as scanning probes[10] and hydrogen-storage materials[11−13] have also been demonstrated. Extensive experimental and theoretical efforts are being pursued to explore SWNT's electronic, optical, vibrational, and mechanical properties.[3,4]

An ideal SWNT can be viewed as a graphene sheet rolled up into a seamless cylindrical tube, and it can be uniquely characterized by the roll-up vector $\mathbf{C_h} = n\,\mathbf{a_1} + m\,\mathbf{a_2} \equiv (n, m)$, where $\mathbf{a_1}$ and $\mathbf{a_2}$ are the graphene lattice unit vectors and n and m are integers. Both (n, n) armchair tubes and (n, 0) zigzag tubes are achiral, while other forms of (n, m) are chiral tubes. Theoretical calculations[3,5,14] predict that SWNTs can have distinctively different electronic structures. Figure 1 shows schematically the electronic density of states (DOS) for both metallic and semiconducting carbon nanotubes. There is nonzero electronic density of states around Fermi level in metallic tubes, whereas a semiconducting tube shows a band gap around its Fermi level. These theoretical predictions of the DOS of SWNTs have been confirmed directly by atomically resolved scanning tunneling microscopy and spectroscopy (STM/STS) measurements on individual tubes.[15−17]

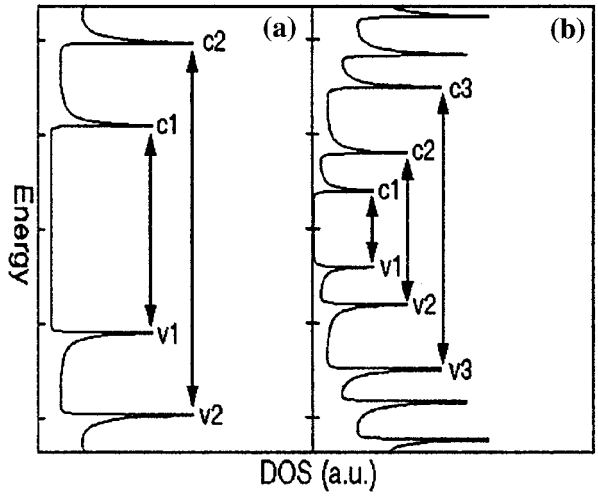

Figure 1. Schematic diagram of electronic density of states for (a) metallic and (b) semiconducting SWNTs. Arrows indicate the optically allowed interband transitions.

The transitions between the mirror-image spikes in the DOS of SWNTs are optically allowed and create excited electronic states,[18,19] as indicated in Figure 1. The interband transition energies are dependent on diameter and chirality of SWNTs.[20,21] They increase with decreasing the diameter of tubes. For SWNTs with a diameter of about 1.3 nm, the energies of

* Author to whom correspondence should be addressed. E-mail: brus@chem.columbia.edu.

10.1021/jp003081u CCC: $20.00
Published on Web 01/19/2001

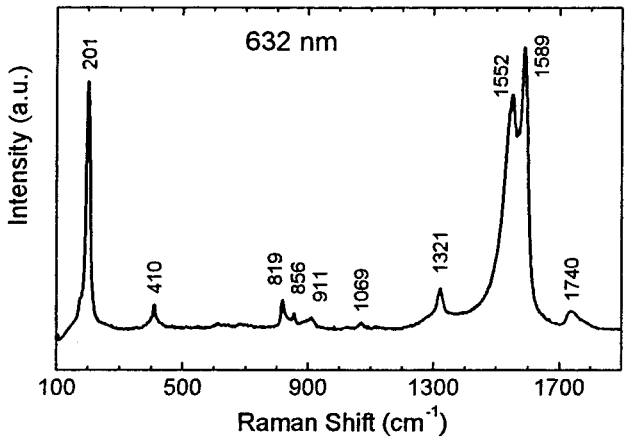

Figure 2. Raman spectrum of a single SWNT bundle obtained by using backscattering confocal Raman microscopy with 20 kW/cm^2 632 nm excitation.

interband transitions v1 → c1, v2 → c2, and v3 → c3 for semiconducting tubes are ∼0.6, 1.2, and 2.4 eV, respectively, and that for v1 → c1 in metallic tubes is ∼1.8 eV. These transitions were observed in optical absorption spectroscopy[22,23] and electron energy loss spectroscopy (EELS)[24] measurements. They were also shown to be responsible for the resonance enhancement effect in Raman scattering from SWNTs.[18,25] Different excitation energies can selectively excite and probe different tubes in the sample. For example, for SWNTs of ∼1.3 nm diameter, the tangential mode Stokes Raman scattering photon with 647 or 632 nm excitation is in resonance with the interband transition v1 → c1 in the metallic carbon nanotubes. Thus Raman scattering from metallic tubes is the dominant contribution with 647 or 632 nm excitation.

Raman scattering is a valuable tool to investigate the vibrational properties and to characterize the sample of SWNTs.[18] Figure 2 shows a typical Raman spectrum from a single SWNT bundle in the range from 100 to 1800 cm^{-1} taken with 632 nm excitation in the backscattering configuration. There are two phonon modes that give a strong Raman scattering signal: the radial breathing mode (RBM) near 200 cm^{-1} and the tangential carbon stretching mode at ∼1580 cm^{-1}. RBM involves the in-phase motion of all carbon atoms in the radial direction. It is predicted that the RBM frequency depends sensitively on the diameter of tubes, but not on chirality.[26] So Raman scattering measurement is a convenient method to estimate the size distribution of a SWNT sample. On the contrary, the tangential mode frequency depends weakly on the diameter of the tubes. However, its Raman line shape depends strongly on whether the tube is metallic or semiconducting. It is discovered that the tangential mode Raman scattering from metallic SWNTs shows a complex broadened line shape.[18,27] This broadening of Raman line shape has been interpreted to result from coupling between phonon scattering and continuous electronic scattering in metallic tubes.[20] However, the origin of the broadened metallic Raman line shape is still unclear; it has been fit either by a set of Lorentzians[27] or a Breit-Wigner-Fano line shape function.[20]

Whereas numerous electrical transport measurements have been carried out on individual carbon nanotubes and bundles, prior optical measurements, mainly Raman scattering and visible absorption, were taken only on ensemble SWNT samples, in which the optical properties were averaged over size, chirality, and orientation of different individual tubes. There is no way currently to make a SWNT sample of uniform size, chirality, and orientation. To get more insight into the intrinsic properties of this one-dimensional carbon structure, it is important to be able to measure optical properties of single SWNT bundles and even single tubes.

Recently, surface-enhanced Raman scattering (SERS) has been applied to measure Raman spectra from single SWNT bundles,[28−30] but the orientation of the tubes was not resolved in the experiment. Also, the modification of the spectra due to SERS effect is not well understood. We have been able to measure Raman scattering from single SWNT bundles without SERS. In this paper, we report our results on Rayleigh and Raman scattering from single bundles. We observed resonance peaks in the Rayleigh scattering spectrum. Both Rayleigh and Raman scattering were found to depend strongly on the orientation of carbon nanotubes with respect to the incident excitation polarization. We also report that Raman scattering from metallic SWNTs is very sensitive to the processing such as thermal treatment and oxidative doping. A mechanism in which charge transfer affects coupling of phonon with isoenergetic electronic states is proposed for the observed effect. Preliminary results have been previously reported.[31]

Experimental Section

Sample Preparation. SWNT material used in this study was purchased from Tubes@Rice (Houston, TX). This material was prepared using the pulsed laser vaporization method,[32,33] purified by refluxing in 2.6 M nitric acid, and redispersed in Triton X-100 aqueous solution of pH 10.[3,4] The diameter distribution of the tubes ranges from 1.05 to 1.6 nm, and is peaked at ∼1.3 nm. In this material, SWNTs aggregate as long ropes forming an entangled networking structure.[33] To break and shorten SWNT bundles, the original SWNT suspension was filtered through a membrane filter (polycarbonate, pore size 3 μ) and washed with methanol. The "bucky paper" formed on the membrane filter was peeled off and soaked in dimethyl formamide (DMF). A stable suspension of shortened SWNTs and bundles was prepared by sonicating the "bucky paper" in DMF for ∼20 h (hereafter, DMF-20 sample).[35] To prevent severe damage to SWNTs from long time sonication, we find that 2 h sonication is enough to obtain a stable suspension if the "bucky paper" is presoaked in DMF for ∼ 2 weeks (DMF-2 sample). To prepare H_2SO_4/H_2O_2-treated sample, SWNTs were precipitated from the original suspension by addition of methanol and subsequent centrifugation. They were then sonicated in a mixture of H_2SO_4 and H_2O_2 (96% H_2SO_4:30% H_2O_2 = 4:1) for 30 min. After being filtered with a polyester membrane filter (pore size 0.5 μ) and washed with deionized water, they were redispersed in DMF with the aid of slight sonication (H_2O_2 sample). A HP 8453 diode array UV−Vis−NIR spectrometer was used to measure the optical extinction spectrum of SWNT suspension.

It has been demonstrated that SWNTs tend to adsorb onto surfaces covered with $-NH_2$ groups.[36] This property has been utilized to pattern and tailor carbon nanotubes onto surfaces.[35,37,38] We used the same deposition method to put SWNTs onto glass and quartz coverslips for optical measurements. The coverslips were functionalized with $-NH_2$ group by soaking them in 1.5 mM solution of 3-aminopropyltriethoxysilane in chloroform for 30 min. They were washed in chloroform and isopropane and blown dry with nitrogen. One drop of diluted SWNT suspension in DMF was put on the $-NH_2$ coverslip for 5 min. The coverslip was then rinsed in methanol and blown dry. An atomic force microscope (AFM) (Digital Instruments Nanoscope IIIa) was used to characterize the coverslips deposited with SWNTs. Figure 3 shows a typical AFM image of DMF-20 SWNTs adsorbed on an $-NH_2$ functionalized glass

Figure 3. A typical AFM height image of SWNTs deposited on an $-NH_2$ functionalized glass coverslip. The *z* range is 10 nm.

coverslip. After sonication in DMF, SWNT entangled networking structure was broken into individual short bundles and tubes. The shortened bundles have an average length and height of 3 μm and 10 nm, respectively, and contain ~100 tubes. The sample adsorbed on $-NH_2$ functionalized coverslips is very clean, as can be seen from the AFM image. These coverslips deposited with SWNTs were used for both Rayleigh and Raman scattering measurements on individual SWNT bundles.

Alternatively, a 1000 mesh bare Cu TEM grid (Ted Pella) was used as a substrate. A few drops of SWNT suspension were spin cast onto Cu grid. Raman scattering were measured from SWNT bundles crossing over the ~19 μm holes of the Cu grid. However, unlike quartz coverslip substrate, bare TEM grid is only suitable to deposit long SWNT bundles.

Optical Measurements. Thick bundles on the coverslip can be observed using an optical microscope with dark field illumination of white light, or with grazing incidence of laser light. Rayleigh scattering spectra from individual bundles were measured with a Nikon inverted optical microscope. The white light from a 300 W tungsten lamp was focused to the sample by a dark field condenser (NA 0.95−0.80). The scattering light from individual bundles was collected by a 100× oil-immersion microscope objective with adjustable NA (NA set at 0.7), focused onto the entrance slit of a spectrometer (Spex 280), and recorded by a liquid nitrogen cooled CCD camera. The recorded scattering spectra were corrected by normalizing with respect to the emission spectrum of the tungsten lamp recorded with the same setup. A polarizer was used to change the polarization of the incident white light. The sample stage can be rotated to adjust the orientation of SWNT bundles. We observed strong polarization dependence of Rayleigh scattering from SWNT bundles, and this was employed to sort out optically the SWNTs from dust particles.

Raman spectra from individual SWNT bundles were measured with the same optical microscope. As shown schematically in Figure 4a, for SWNTs deposited on coverslips, grazing incidence geometry was employed, with an incidence angle of about 30° relative to the coverslip surface. Randomly polarized 632 nm light from a HeNe laser (Spectra Physics, 4.5 mW) or vertically polarized 457 nm light (50 mW) from an Ar^+ ion laser (Coherent) was focused to the sample by a $f = 1.0$ cm triplet lens, with a focusing spot size of ~5 μ. Typical excitation intensities are ~20 kW/cm^2 for 632 nm and ~200 kW/cm^2 for

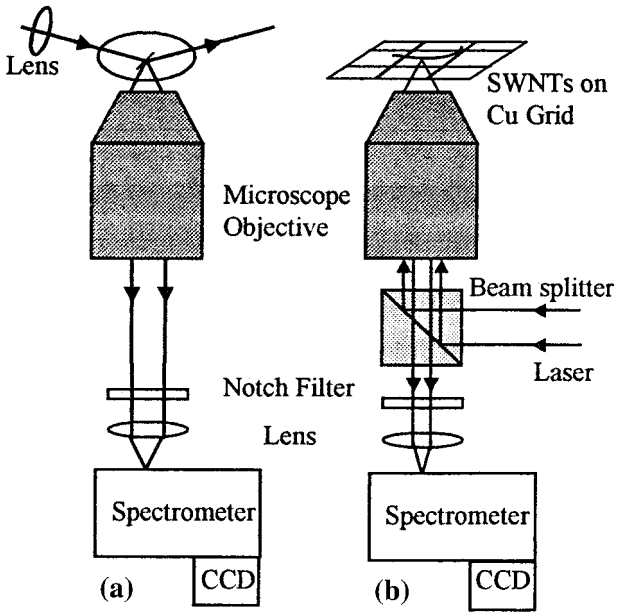

Figure 4. Schematic diagrams of experimental setup for (a) grazing incidence and (b) backscattering confocal Raman microscopy.

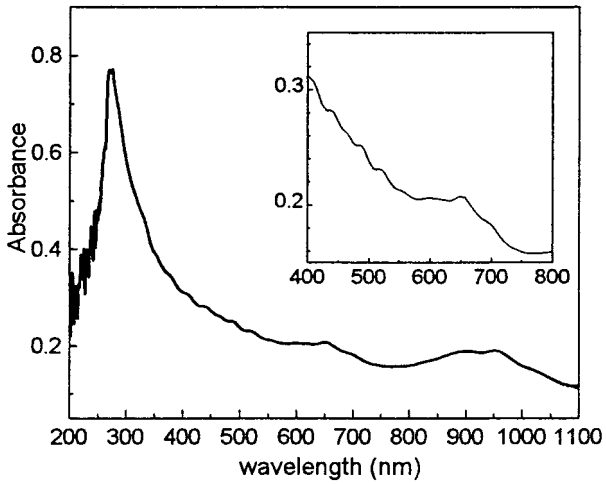

Figure 5. UV−Vis−NIR extinction spectrum of the DMF-20 SWNT sample. Inset shows the close-up of the visible spectrum.

457 nm. The Raman scattering collection angle is about 120°. Notch filters (Kaiser optics) were mounted in front of the spectrometer to reject the Rayleigh scattering laser lines.

Backscattering confocal Raman microscopy was employed to measure Raman spectra from SWNT bundles suspending in air over the holes of the TEM grid in order to eliminate substrate scattering background, as shown schematically in Figure 4b. To be able to measure anti-Stokes Raman scattering, a cube beam splitter can be used replacing a dichroic mirror. A laser beam was focused to one ~0.5 μ spot on a bundle by a 125× air objective (NA 0.8). Excitation intensity can be changed from ~2 kW/cm^2 to ~200 kW/cm^2 by using neutral density filters. Backscattered Raman light was collected by the same objective and focused to the spectrometer. SWNT bundles could be found by using dark field optical microscopy or by moving the grid until a scattering spot from the laser hitting the suspended bundle was observed through the eyepieces.

Results

Optical Absorption Of SWNT Suspension. The UV−Vis−NIR optical absorption spectrum of the DMF-20 SWNT suspension is shown in Figure 5. Unlike Chen et al.'s result,[22]

in which no peaks were observed in the visible range, we observed many absorption peaks in the spectrum, probably because of the narrow size distribution in SWNT samples made by laser vaporization.[33] These absorption peaks can be ascribed to the interband transitions between the mirror image spikes in DOS of SWNTs.

From electronic band theory, the interband transition energies for v2 → c2 and v3 → c3 transitions in semiconducting tubes, and v1 → c1 and v2 → c2 transition in metallic tubes are approximated by[19,39]

$$E^{S}_{22}(d_t) = 4a_{c-c}\gamma_0/d_t$$

$$E^{S}_{33}(d_t) = 8a_{c-c}\gamma_0/d_t$$

and

$$E^{M}_{11}(d_t) = 6a_{c-c}\gamma_0/d_t$$

$$E^{M}_{22}(d_t) = 12a_{c-c}\gamma_0/d_t$$

respectively. Here a_{c-c} is the nearest-neighbor carbon−carbon distance, which is taken to be 1.44 Å for a SWNT. γ_0 is the nearest-neighbor carbon−carbon interaction energy, and d_t is the diameter of a SWNT. The SWNT sample used in this study has a mean diameter of ∼1.3 nm.[33,34] If we take γ_0 to be 2.9 eV,[21] E^{S}_{22} (d_t), E^{S}_{33} (d_t), E^{M}_{11} (d_t), and E^{M}_{22} (d_t) can be calculated to be ∼1.3, 2.6, 1.9, and 3.8 eV, respectively. These interband transition energies of single tubes have been directly measured by scanning tunneling microscopy and spectroscopy.[15−17] Experimental values agree well with theoretical predictions. On the basis of this theoretical prediction, the absorption peaks between 800 and 1100 nm can be assigned to the second interband transitions v2 → c2 in semiconducting tubes, whereas the peaks around 650 nm are ascribed to the first interband transitions v1 → c1 in metallic nanotubes. Those weak peaks between 550 and 300 nm superimposed on an absorption continuum can be due to the v3 → c3 transitions in semiconducting tubes and v2 → c2 transitions in metallic tubes. The energy of the strong ∼270 nm peak is close to the π plasmon frequency ∼5 eV in carbon materials such as graphite, C_{60}, and SWNTs.[24] Its intensity is found to increase with time when the sonicated SWNTs are kept in DMF. We filtered the suspension, and found that most of the intensity of this peak remained in the filtrate, not in the redispersed SWNT suspension. It might result from some fullerene molecules dissolved from the damaged nanotubes.[40]

Rayleigh Scattering Spectra. Figure 6, parts a and b, show two typical visible Rayleigh scattering spectra of individual DMF-20 SWNT bundles. The typical Rayleigh scattering spectrum of single bundles is similar to the visible absorption spectrum of SWNT suspension shown in the inset of Figure 5. Some resonance peaks are observed superimposed on a scattering continuum. As in the optical absorption spectrum, these resonance peaks are due to the optically allowed interband transitions in SWNTs. The peaks around 650−700 nm in the Rayleigh scattering spectrum can be assigned to v1 → c1 interband transition in metallic tubes, and those peaks at higher energies can be assigned to v3 → c3 transition in semiconducting tubes.

In the approximately 30 bundles we examined, most of them show the typical Rayleigh scattering spectra as in Figure 6, parts a and b. So most of the bundles have similar tube composition, which represents that of the bulk sample. Occasionally we observed Rayleigh scattering spectra that are quite different from the typical spectrum. Two of the examples are shown in Figure 6c for one large bundle and 6d for one small bundle. In Figure 6c a strong semiconducting peak near 550 nm and a weak metallic peak at 650 nm are observed, suggesting that this bundle is mainly composed of semiconducting nanotubes. On the contrary, the spectrum in Figure 6d exhibits a strong resonance peak around 700 nm, implying that metallic tubes are enriched in this specific bundle. Spectrum 6d is characteristic of the three thin bundles we observed. Our observation that metallic tubes seem to be enriched in thin bundles is consistent with STM studies showing that the helicity distribution of SWNTs in bundles shifts from favoring zigzag (n, 0) direction in an unetched sample to a more uniform distribution in a sonicated sample.[17]

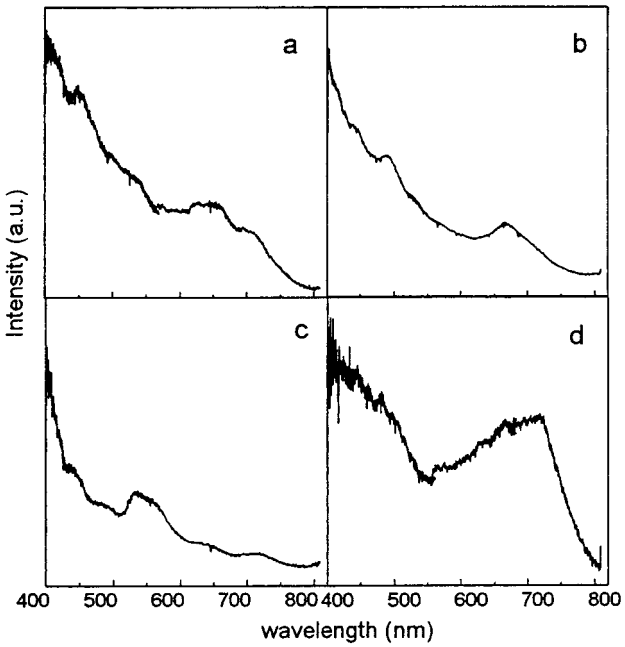

Figure 6. Rayleigh scattering spectra from four different SWNT bundles. (a) and (b) are typical spectra observed. Occasionally spectra (c) for a thick bundle and (d) for a thin bundle different from typical spectra are observed.

The Rayleigh scattering spectrum of a SWNT bundle depends strongly on the polarization of the incident white light. Figure 7 shows the different Rayleigh scattering spectra from one same bundle with polarized excitation but with unpolarized detection. First, when the incident light polarization is parallel to the tube axis, the Rayleigh scattering spectrum shows the resonance peaks. However, these resonance peaks disappear completely when the incident light polarization is perpendicular to the tube axis. Second, the continuous scattering from the bundle is about 3−6 times weaker for perpendicular polarization than for polarization parallel to the tube axis. This polarization dependence of Rayleigh scattering suggests that the optical transition dipoles in SWNTs are along the tube axis, which agrees with theoretical predication.[41] Tang et al. observed similar polarization dependence in absorption measurement on SWNTs formed in channels of $AlPO_4$-5 single crystal.[42]

Raman Scattering from Single Bundles. Consistent with ensemble measurement,[18,25] Raman spectra from individual SWNT bundles clearly demonstrate the diameter selective resonance effect for different excitation energies. Figure 8 shows both the radial breathing mode (RBM) and the tangential mode Raman scattering from a typical single bundle obtained using grazing incidence Raman microscopy. The RBM Raman line

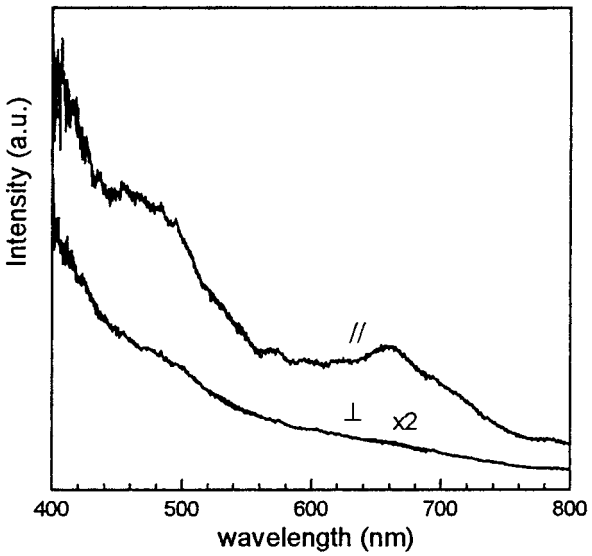

Figure 7. Polarization dependence of Rayleigh scattering spectrum from a single bundle, with incident polarization either parallel (top) or perpendicular (bottom) to the bundle axis.

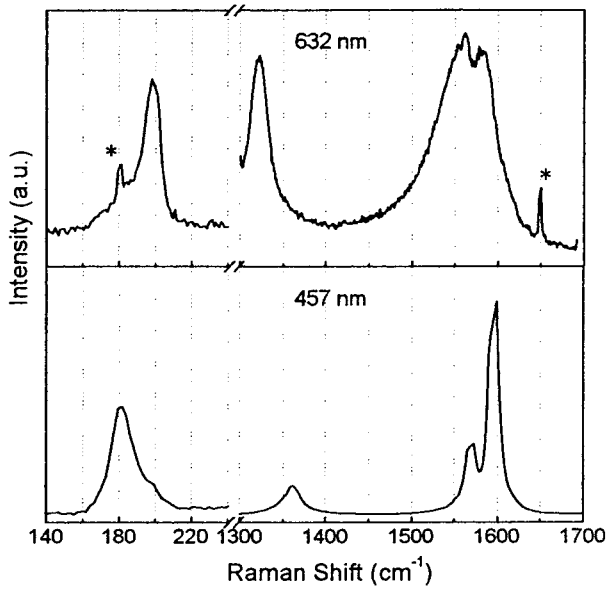

Figure 8. Typical breathing mode and tangential mode Raman spectra from a single DMF-20 bundle deposited on a quartz coverslip. Spectra were taken using grazing incidence Raman microscopy with 20 kW/cm^2 632 nm and 200 kW/cm^2 457 nm excitation. The peaks marked with * are laser plasma lines.

shows a peak around 198 cm^{-1} with 632 nm excitation. When excited by 457 nm light, the same bundle shows the main RBM peak at 182 cm^{-1}. This diameter selective effect has been interpreted to result from the resonance effect associated with the interband transitions in SWNTs.[18,25] The optically allowed interband transitions are dependent on diameter and chirality of the tubes. Thus SWNTs of different diameters will be resonantly excited by different excitation energies, and show different RBM Raman peak positions, which are dependent sensitively on the diameter of the tubes.

Theoretical calculations[26,43,44] predict that the RBM frequency depends only on the diameter of a SWNT; they are shown to be related by

$$\nu\ (\mathrm{cm}^{-1}) = 223.75\ (\mathrm{cm}^{-1}\cdot\mathrm{nm})/d\ (\mathrm{nm})$$

This equation has been used to estimate the size distribution of a SWNT sample from an RBM Raman spectrum.[43,44] However, intertube interaction in bundled SWNTs has been shown to upshift the RBM frequency by 15 cm^{-1} or 8.5% in calculations[45−47] of vibrational properties of bundled SWNTs. The effect of the intertube interaction is not included in the above equation. In our experiment, Raman spectra from individual bundles were measured, each containing about 100 tubes. Also the quartz substrate may have the similar effect on RBM frequency of SWNTs. We then use the equation

$$\nu\ (\mathrm{cm}^{-1}) = 223.75\ (\mathrm{cm}^{-1}\cdot\mathrm{nm})/\mathrm{d}\ (\mathrm{nm}) + 15\ \mathrm{cm}^{-1}$$

for bundled SWNTs to estimate the diameter of SWNTs in the bundle. In Figure 8, SWNTs contributing to the 632 nm RBM Raman signal have a mean diameter of 1.22 nm, to which (9, 9) metallic tube is closest. SWNTs selectively excited by 457 nm photons have a mean diameter of 1.33 nm, close to that of (17, 0) semiconducting tube. The SWNT diameters estimated from RBM frequency are in good agreement with the value determined from TEM and XRD measurements.[33,34]

The tangential mode Raman scattering shows distinctively different line shapes with 632 and 457 nm excitation, similar to ensemble Raman measurements.[18,25] The tangential mode Raman line is broadened with 632 nm excitation compared with 457 nm excitation, and a strong Raman line at 1550 cm^{-1} appears. The 1590 cm^{-1} Raman line has been recently identified as coming from semiconducting tubes in the bundle.[48] Raman scattering with 632 nm excitation is mostly contributed by metallic tubes in the bundle. This broadened Raman line shape at 1550 cm^{-1} is believed to arise from coupling between phonon scattering and the electronic scattering in metallic tubes.[20] It's specific to metallic SWNTs because only metallic tubes have a nonzero electronic density of states (DOS) around Fermi energy level. This coupling mechanism is supported by the fact that the broadened 1550 cm^{-1} mode from a thin bundle can be well fitted by a Breig-Wigner-Fano (BWF) line shape function,[49] which will be discussed below.

Figure 8 also implies that there is a wide size distribution of single tubes even in a single bundle. Our typical Raman spectra from thick single bundles are similar to ensemble spectra measured on laser-ablated SWNTs with 632 nm[47] and 457 nm[25] excitation. Just as revealed in Rayleigh scattering spectra, the size distribution in a typical bundle is wide and representative of that in ensemble sample. This is consistent with STM characterizations, which show that many different (*n*, *m*) tubes can be found in a bundle.[17]

Thin bundles occasionally show simpler and sharper spectra. The sharpest RBM Raman spectrum is shown in Figure 9, which is obtained with 457 nm excitation. It contains three resolved peaks; each peak is fitted with a Lorentzian function. The fitted peak frequencies and line widths are listed in Table 1, along with possible (*n*, *m*) assignments for each peak. The fitted Raman line width for 218 cm^{-1} peak is 7 cm^{-1}; the experimental resolution is 4 cm^{-1}. This line width is smaller than that of 8.4 cm^{-1} used in fitting RBM Raman peaks for ensemble sample.[25] Also it is in the RBM line width range 6−10 cm^{-1} obtained for small bundles or single tubes using SERS.[28] But it is about twice the line width value of 4 cm^{-1} used in simulating RBM Raman spectra by Milnera et al.[47]

The tube composition varies from bundle to bundle. Shown in Figure 10 are the Raman spectra of four different bundles with both 632 and 457 nm excitation. With 457 nm excitation, from Figure 10, part a to part d, the dominant RBM peak shifts to high energy, suggesting that the corresponding nanotube size distribution in the bundles shifts from thick tubes to thin tubes. Note that although 457 nm RBM Raman scattering shows more

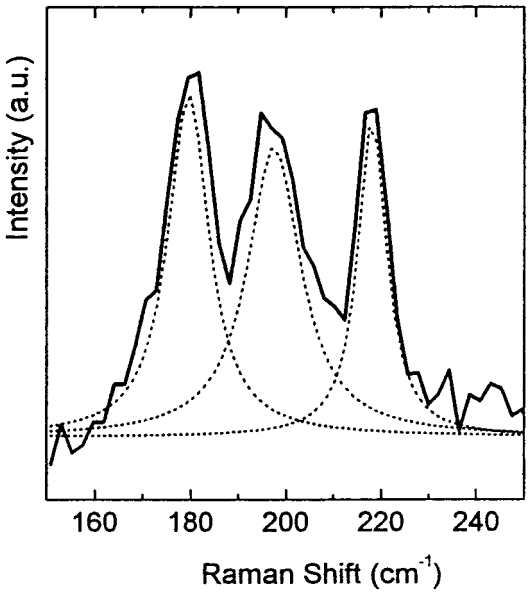

Figure 9. The sharpest radial breathing mode Raman lines obtained from a single bundle with 457 nm excitation. The dotted curves are Lorentzian fits to the three resolved Raman peaks.

TABLE 1: Fit Peak Positions and Lorentzian Line Widths for the RBM Raman Lines in Figure 9[a]

Raman line (cm^{-1})	Lorentzian width (cm^{-1})	calcd. diameter (nm)	possible (*n*, *m*)
180	10	1.36	(15, 4), (11, 9), (12, 8)
200	13	1.23	(14, 3), (11, 7), (16, 0)
218	7	1.10	(14, 0), (13, 2), (10, 6)

[a] The calculated diameters of the corresponding tubes are also listed, with possible (*n*, *m*) assignments. Semiconducting tubes are assumed to contribute to the Raman lines.

peaks and larger variation, it remains similar for all the bundles with 632 nm excitation. It seems that 457 nm photon can be in resonance with more nanotubes of different diameters while 632 nm light can only excite nanotubes of a specific diameter. Also note that in Figures 8 and 10, the 457 nm tangential mode Raman scattering shows the same line shape for all the bundles. However, for 632 nm excitation, the 1550 cm^{-1} mode shows large variations in its line shape and relative intensity. This large variation is closely related to the origin of the broadening of the tangential mode Raman scattering in metallic SWNTs, as discussed below. We notice that in our measurement the broadened metallic peak appears at ~1550 cm^{-1} instead of 1540 cm^{-1} observed in ensemble measurement on the same type of sample.[25,27]

In the Raman spectra shown above, the metallic SWNTs exhibit a very strong disorde-induced Raman peak around 1320 cm^{-1}. The disorder mode is believed to result from disorder structure and symmetry lowering effects in carbon materials.[18] For example, small graphite particles show a stronger disorder Raman peak than large graphite particles.[50] In our case, a 20 h sonication creates a strong disorder Raman peak in metallic tubes. A 2 h sonication in a presoaked sample shows a weaker disorder peak in Figure 11. We also note that in Figure 10 the disorder peak intensity is correlated with that of a Raman component at ~1610 cm^{-1}. This Raman shoulder shows up only in the bundle with strong disorder mode Raman intensity. However, the semiconducting tubes show a weak disorder mode signal at 1361 cm^{-1} with 457 nm excitation even in 20 h sonicated short bundles. It seems that metallic SWNTs are more likely to be damaged by sonication than the semiconducting tubes. One possible explanation for this observation is that in our sample the metallic tubes have a smaller diameter than the semiconducting tubes, as evidenced from the typical Raman spectra shown in Figure 8. Small diameter tubes have more strain energy[51] and are thus more likely to be damaged by ultrasound illumination. Also, the curvature elastic energy in straight armchair tubes (which are metallic) has been recently predicted[52] to be higher than that in zigzag tubes with same diameters, consistent with our observation. However, more study

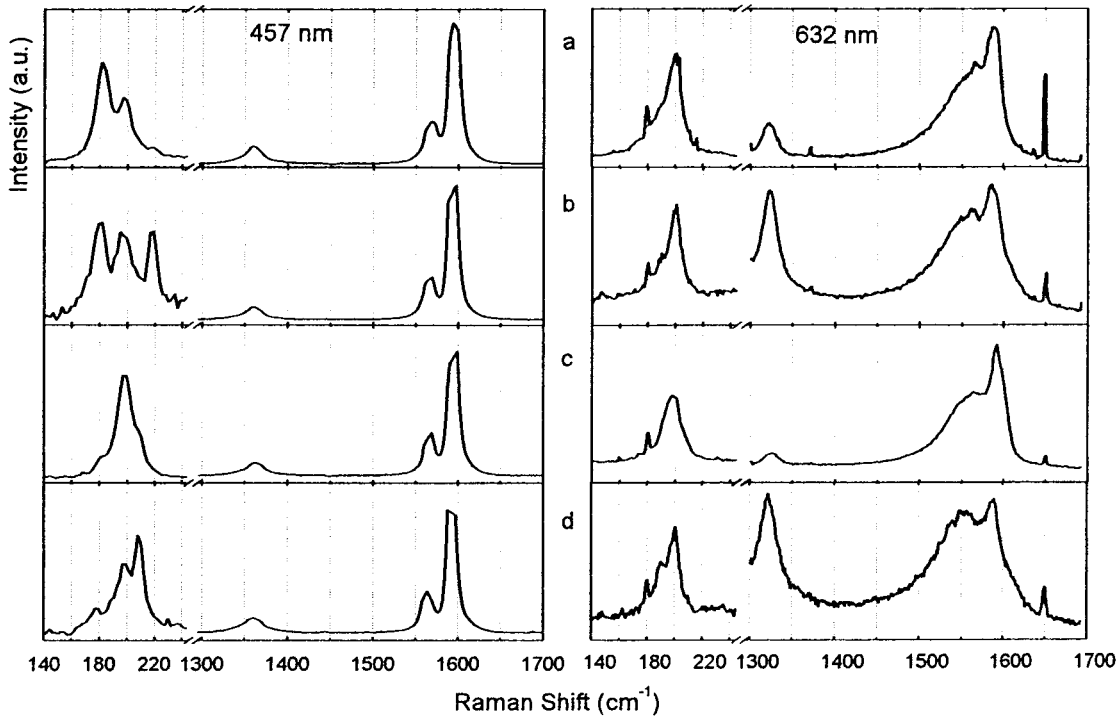

Figure 10. Variation of Raman spectra from four different DMF-20 SWNT bundles. The RBM spectrum with 457 nm excitation for (b) is the same as Figure 9. Note that 457 nm breathing mode and 632 nm tangential mode Raman show large variation from bundle to bundle.

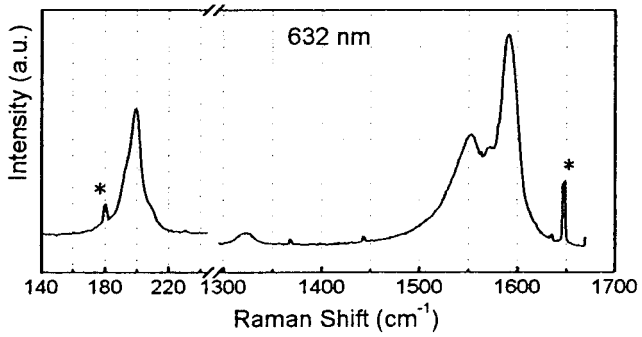

Figure 11. Raman spectrum from a DMF-2 bundle, showing the weak disorder mode Raman peak. The peaks marked with * are laser plasma lines.

is needed to fully understand the origin of the disorder Raman mode in SWNTs.

Raman Spectra from Thin Ropes. In the Raman scattering measurement on SWNTs deposited on a coverslip, the coverslip itself produces continuous Stokes shifted scattering background. In fact with 457 nm excitation, the Raman signal from SWNT bundles in the 300−700 cm^{-1} region is buried in the strong scattering background from the quartz coverslip. To obtain a clean Raman spectrum from single bundles, especially to characterize the broadened tangential mode Raman line shape in metallic SWNTs, we carried out Raman scattering measurements on ∼20 μ long bundles crossing over the holes of the TEM grid using confocal Raman microscopy, thus eliminating scattering background from the substrate.

One typical clean Raman spectrum from a single bundle suspending in air is shown in Figure 2. The signal-to-noise ratio is so high that even those weak Raman peaks in the 300−1200 cm^{-1} region are clearly observed. Figure 12a is another clean spectrum from a single bundle taken with 632 nm excitation at 30 kW/cm^2 intensity. The high signal-to-noise ratio enables us to resolve several weak breathing mode peaks in both the Stokes and anti-Stokes Raman spectrum.

With this setup it is possible to take a Raman spectrum from thin bundles. Figure 12, parts b and c, are unpolarized Raman spectra taken from two different thin bundles. These thin bundles could not be seen by using the dark field optical microscope. Instead, they were found by moving the TEM grid and observing the Rayleigh scattering from the focused laser hitting the bundles. In Figure 12b, the spectrum, obtained with 457 nm excitation, is similar to that in thick bundles. However, in Figure 12c the tangential mode Raman spectrum of a thin bundle with 632 nm excitation is quite different than that from thick bundles. The two peaks near 1600 cm^{-1} are well resolved, and it has a strong broadened 1550 cm^{-1} peak. Following Kataura et al.,[20] the 1550 cm^{-1} peak can be well fitted with a Breig-Wigner-Fano (BWF) line shape function

$$I(\omega) = I_o\{1 + (\omega - \omega_o)/q\Gamma\}^2/\{1 + [(\omega - \omega_o)/\Gamma]^2\}$$

where I_o, ω_o, Γ, and q, indicated in Figure 12c, are intensity, renormalized frequency, broadening parameter, and the asymmetry parameter, respectively. The agreement with BWF function supports the previous interpretation of broadening of the tangential mode Raman scattering from metallic tubes.[20]

Sensitive Raman Scattering from Metallic SWNTs. When we were studying power dependence of Raman spectra from single bundles using confocal Raman microscopy with 632 nm excitation, we found that the tangential mode Raman scattering underwent an irreversible change after high power laser irradiation, as shown in Figure 13, which displays the Raman spectra in the 1270−1670 cm^{-1} range for a single bundle. At low excitation intensity 3.3 kW/cm^2, there are mainly two peaks: one at ∼1560 cm^{-1} and one at ∼1590 cm^{-1}. At high excitation intensity 340 kW/cm^2, a new, broad peak at ∼1540 cm^{-1} develops. When the power was lowered to 3.3 kW/cm^2, this new broad peak remains present. We observed this irreversible change in Raman scattering in every bundle studied using confocal Raman microscopy with 632 nm excitation. The Raman spectrum for 632 nm excitation after high power laser irradiation is similar to the ensemble spectrum obtained on the same laser-ablated SWNT sample.[18,25] If we move to a new spot on the same bundle, the original Raman is observed. RBM Raman scattering does not show this large change in our measurements.

One explanation for this irreversible Raman change in metallic tubes is that laser irradiation heats and thus degases SWNT bundles. Rinzler et al. previously used laser irradiation to heat multiwall carbon nanotubes.[53] In our case, SWNT bundles are suspended in air and an excitation laser beam is focused on one spot on the bundles. We previously showed that the laser heats the bundle locally to ∼750 K at 220 kW/cm^2

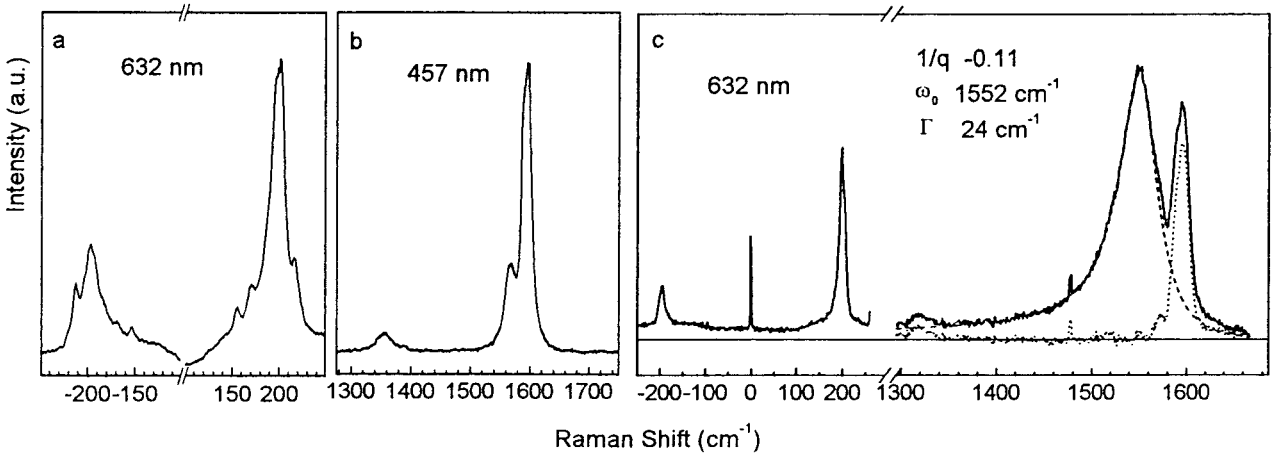

Figure 12. (a) High signal-to-noise ratio Stokes (shown as positive Raman shift) and anti-Stokes (shown as negative Raman shift) Raman spectrum from a single DMF-2 bundle using confocal Raman microscopy with 632 nm excitation. (b) Tangential mode Raman spectrum from a thin DMF-2 bundle with 457 nm excitation. (c) Raman spectrum from another thin DMF-2 bundle with 632 nm excitation (solid curve). The broadened 1550 cm^{-1} peak is well fit by a BWF line shape function (dashed curve), with parameters indicated in the figure. The dotted curve is the remaining spectrum after subtracting BWF fit from the experimental spectrum.

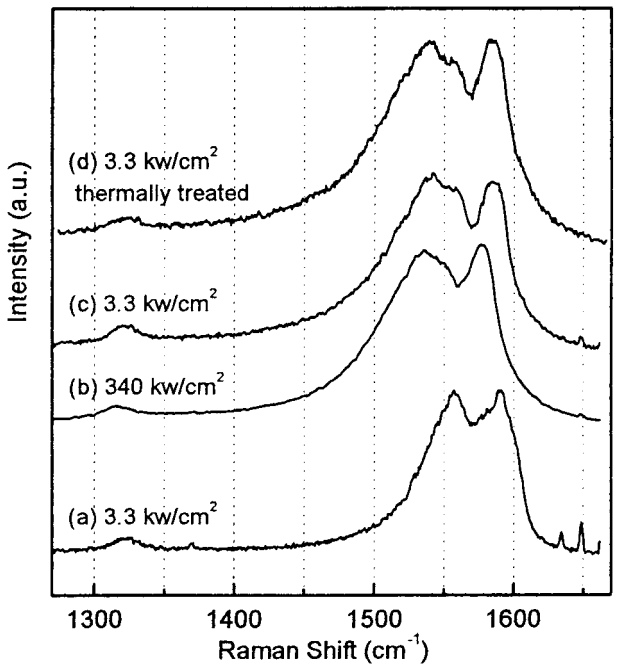

Figure 13. Tangential mode Raman spectra from a DMF-2 SWNT bundle taken consecutively at low, high, and low 632 nm excitation intensities (from a to c). After high power laser irradiation the tangential mode Raman scattering underwent an irreversible change. (d) is a typical Raman spectrum from a single bundle after heating at 400 °C in Ar.

632 nm excitation intensity.[31] To test whether the observed large irreversible change in tangential mode (TM) Raman scattering is due to sample heating, we put the Cu grid with SWNTs in a furnace and heated the sample at 400 °C for 2 h in flowing Ar. Then Raman scattering was measured again with low power 632 nm excitation. Thermal treatment had the same effect on Raman scattering as high power laser irradiation, as shown in Figure 13. After heating the sample, we obtained the tangential mode Raman spectra similar to those after high power laser irradiation. In our experiment, locally heating the bundle in air by focused laser beam does not burn SWNTs, because the damaged open ends of SWNTs are not irradiated and heated by the laser, which are in contact with copper metal grid.

The H_2O_2 SWNT bundles show similar irreversible change in TM Raman scattering for 632 nm after high power irradiation, as shown in Figure 14. First note the distinctively different TM Raman spectrum of the H_2O_2 sample compared with that of the DMF-2 sample in Figure 13. The 1550 cm^{-1} Raman line is strongly suppressed, and the Raman peaks are narrower and more like the Raman spectrum from semiconducting tubes. After high intensity 220 kW/cm^2 laser irradiation, the characteristic 1540 cm^{-1} peak appears and the whole spectrum gets broader. After we heat the H_2O_2 sample at 400 °C, the Raman spectrum is same as that shown in Figure 13.

As shown in Figure 13, the disorder-induced Raman peak at 1325 cm^{-1} is weak, and there is no change in its intensity after heating the sample. So the large change observed in TM Raman scattering from metallic SWNTs is not due to structural annealing upon heating. We propose that the observed sensitivity of TM Raman scattering in metallic SWNTs to processing conditions is due to the SWNT−adsorbate interaction. Molecules such as NO_2 and NH_3 are known to adsorb on SWNTs at room temperature.[54] We expect that in our case oxidizing molecules can also adsorb into SWNT bundles during the processing. They are still present in the bundle after SWNTs are deposited on the substrate. Comparing the TM Raman scattering from metallic

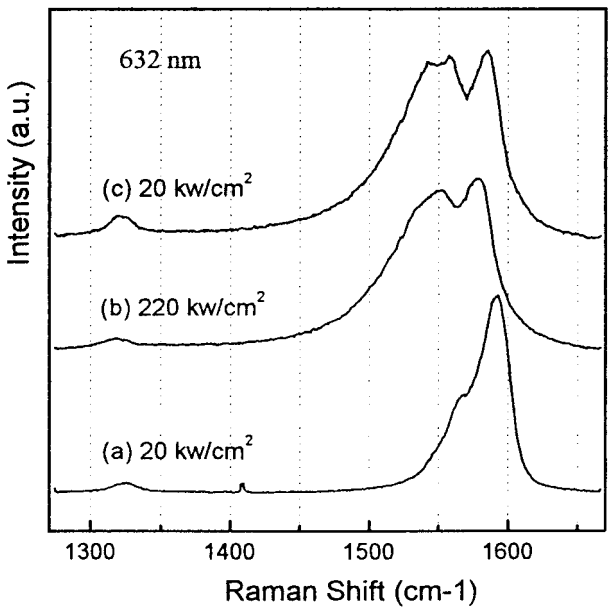

Figure 14. Same as Figure 13 but with a H_2SO_4/H_2O_2-treated SWNT bundle.

tubes in DMF-2 sample with that in H_2O_2 sample, we see that oxidation by H_2SO_4/H_2O_2 strongly suppresses the characteristic metallic peak at 1540 cm^{-1}. Note that the original SWNT sample was purified by refluxing in nitric acid, an oxidant weaker than H_2SO_4/H_2O_2.[34] Exposure to nitric acid would suppress the metallic Raman peak at 1540 cm^{-1} to a less extent than H_2SO_4/H_2O_2, as observed for DMF-shortened bundles shown in Figures 10 and 13. However, after heating both the original (HNO_3-treated) and the H_2SO_4/H_2O_2-treated SWNT bundles, we obtain the strong, characteristic 1540 cm^{-1} peak.

If we expose the thermally treated SWNT bundles to Br_2 vapor briefly for 2 min at room temperature, the 1540 cm^{-1} metallic Raman peak is strongly suppressed when measured at low power 632 nm excitation, similar to the H_2O_2 sample. It recovers after the excitation intensity is increased. All these observations prove that the TM Raman scattering from metallic SWNTs is very sensitive to the SWNT-adsorbate interaction, and that the observed large change in TM Raman scattering after heating the SWNT sample is due to degassing.

Polarized Raman Scattering. Polarized Raman scattering measurement was carried out on a single bundle deposited on the quartz coverslip with grazing incidence of 457 nm light. The scattering configuration is schematically shown in the inset to Figure 15. The sample stage was rotated to change the orientation of the bundles relative to the excitation polarization. A scrambler was put in front of the spectrometer. Figure 15 shows the Raman signal of a same bundle at (//, //), (//, ⊥), and (⊥, ⊥) configurations, where the first and the second symbol in the parentheses denote the polarization of excitation light and the detected Raman scattering, respectively, with // and ⊥ being parallel and perpendicular to the tube axis, respectively. Both breathing mode and tangential mode show strongest Raman signal in the (//, //) configuration. When the excitation polarization is parallel to tube axis, the Raman scattering polarized along the tube axis is about 40 times stronger than that polarized perpendicular to the tube axis for this particular bundle.

Similar results were obtained with 457 and 632 nm excitation in backscattering geometry, with intensity ratio of parallel Raman to perpendicular Raman varying from ∼20 to more than 100 (undetectable perpendicular Raman scattering). Some of this variation from bundle to bundle may represent varying

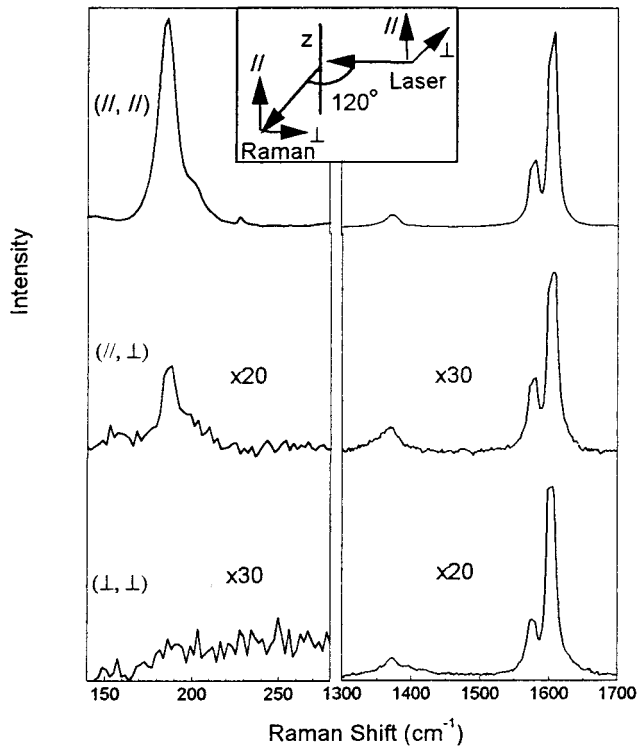

Figure 15. Polarized Raman scattering from a single DMF-2 bundle on quartz coverslip using grazing incidence Raman microscopy with 200 kW/cm^2 457 nm excitation. Inset shows schematically the scattering configuration. The bundle is along the *z* direction.

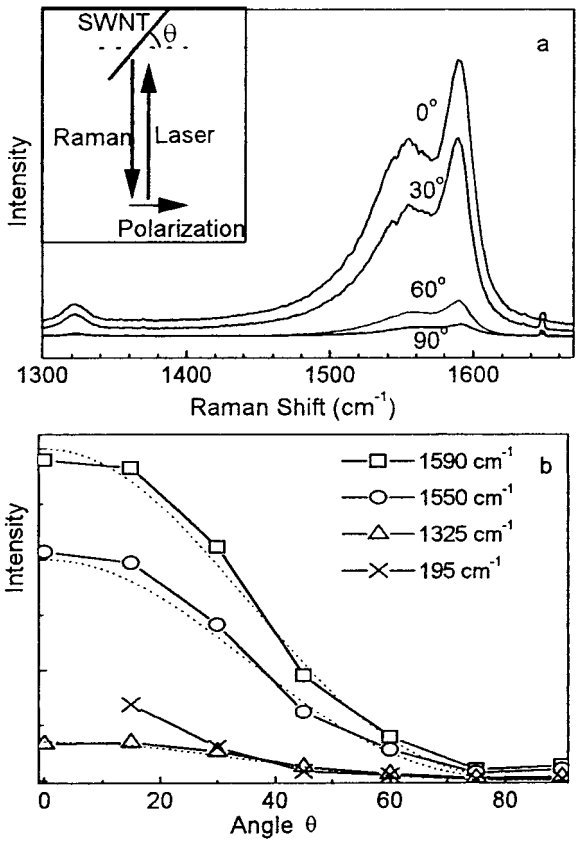

Figure 16. (a) Angular dependence of Raman scattering from a single DMF-2 bundle using backscattering confocal Raman microscopy with 45 kW/cm^2 632 nm excitation. Inset shows the bundle is rotated to change its angle θ with respect to the laser polarization. (b) Plot of four Raman line intensities versus the angle θ. Dotted curves are fits with a $\cos^3\theta$ function.

bundle curvature; that is, the bundles are not perfectly straight over the laser spot size.

As predicted by theory,[3] the RBM mode behaves as A_{1g}. The nonresonant Raman active tangential modes are predicted to consist of three almost degenerate modes with A_{1g}, E_{1g} and E_{2g} symmetry, respectively.[3] Group theory predicts that A_{1g} mode is allowed in (//, //) and (⊥, ⊥) configurations, but it is forbidden in the (//, ⊥) configuration. The E_{1g} mode is only allowed in the (//, ⊥) configuration, while the E_{2g} mode is allowed only in the (⊥, ⊥) configuration.[55] However, simple resonant Raman theory[56] shows that both E_{1g} and E_{2g} modes should be weak compared with the A_{1g} mode. From our measurement, in the semiconductor tangential mode spectra, both the major peak at ~1590 cm^{-1} and the small peak at ~1570 cm^{-1} behave as A_{1g}. Their relative intensity ratio is the same in all bundles. In the 632 nm spectra, both the ~1590 cm^{-1} sharp peak and the ~1540 cm^{-1} broad peak behave as A_{1g}. The sharp ~1590 cm^{-1} peak may come from the semiconducting tubes in the bundle; this question needs further research.

Figure 16 shows the nanotube orientation dependence of Raman scattering from a single bundle measured using confocal Raman microscopy with 632 nm excitation. Excitation polarization and detected Raman polarization were kept parallel to each other while the sample was rotated to adjust the angle between the tube axis and the excitation polarization, as shown in the inset to Figure 16a. To reduce the thermal drifting effect on the Raman intensity, the position of the bundle relative to the laser focusing spot was constantly monitored and adjusted while the data were being collected. The Raman scattering is strongest when the tube axis is parallel to the excitation polarization, which corresponds to the (//, //) configuration. It becomes weaker when the tube axis is closer to being perpendicular to the light polarization, corresponding to the (⊥, ⊥) configuration. We did not observe that the Raman signal decreases to a minimum at ~55° and rises afterward, as observed by Rao et al. with aligned multiwall nanotube sample.[57] Also we observed that the Raman lines in Figure 16a reserve their relative intensity, and intensity changes of these Raman lines with rotation angle θ can be approximately described by a $\cos^3\theta$ function. All these lines behave like A_{1g} modes.

Discussion

Polarization Dependence of Rayleigh Scattering. Our results demonstrate that the resonance peaks in the Rayleigh scattering spectrum are suppressed when the incident light polarization is perpendicular to the nanotube axis, most obviously for metallic tube v1 → c1 interband transition peak around 700 nm. Thus the optical transition dipole moment in carbon nanotubes is orientated parallel to the tube axis.

Saito et al. calculated the electronic band structure of carbon nanotubes within the zone-folding model.[14] Take (5, 5) metallic tube as an example. It belongs to D_{5d} point group, and the v1 → c1 interband transition is from e_{1g} to e_{1u}.[3] From group theory, for D_{5d} point group we have

$$e_{1g} \otimes e_{1u} = a_{1u} + a_{2u} + e_{2u}$$

An optically allowed transition requires that $\langle i|\mathbf{p}|f\rangle \neq 0$, where **p** is the dipole moment operator, and i and f are the two states involved in the transition. Thus i⊗f should contain the same symmetry as **p**. For the D_{5d} point group, *z* belongs to a_{2u} and (*x*, *y*) belongs to e_{1u}. Here *z* is along the tube axis. We see that

$e_{1g} \otimes e_{1u}$ contains a_{2u}, not e_{1u}. So the transition dipole moment must be along *z*, i.e., the tube axis, in order for the v1 → c1 interband transition to be optically allowed.

The optical absorption spectrum of carbon nanotubes has been calculated by Ajiki et al.[41] Their calculations show that optical absorption exhibits strong resonance peaks when the light polarization is parallel to the tube, whereas the resonance peaks are all depressed for light polarization perpendicular to the tube axis. They argued that these resonance peaks disappear almost completely for perpendicular light polarization because of the strong depolarization effect.

Raman Scattering from Metallic SWNTs. The broadening of the tangential mode line shape of metallic SWNTs has been tentatively interpreted as resulting from coupling between phonon scattering and the continuous electronic scattering.[20] But it is not clear whether the broadened line shape can be fitted with a BWF function[20] or with unresolved Lorentzian lines.[27] We find that the broadened 1550 cm^{-1} peak can be fitted very well with a BWF line shape function, supporting the idea that interference between electronic scattering and phonon scattering is involved.[20]

The large change in TM Raman scattering from metallic SWNTs was observed upon degassing and doping with oxidants such as HNO_3, H_2SO_4/H_2O_2, and Br_2. The electric conductance of SWNTs has been shown to be very sensitive to exposure to gases such as NO_2 and NH_3; the large reversible change in conductance observed was interpreted to result from charge transfer doping.[54] Note that an upshift in the tangential mode frequency in semiconducting tubes heavily doped with Br_2 has been reported.[58] We propose that a similar charge transfer between SWNTs and adsorbed oxidizing molecules is responsible for our observed effects in metallic Raman scattering. Apparently the lowered Fermi level in SWNTs due to oxidative doping causes the weaker 1540 cm^{-1} metallic line in HNO_3-treated sample and the strong suppression of 1540 cm^{-1} Raman component in H_2SO_4/H_2O_2-treated and Br_2-exposed SWNT bundles.

One might suggest two possible mechanisms for the effect of charge transfer on Raman scattering from metallic nanotubes. One involves the change in resonant electronic absorption properties of SWNTs upon chemical doping, which has been reported by some groups.[59,60] However, we observed that H_2SO_4/H_2O_2 oxidation produced no apparent change in the visible metallic electronic transition at low resolution, as observed in extinction spectra of SWNT suspensions. The resonance absorption peak at ~650 nm due to metallic tubes still exists in the H_2SO_4/H_2O_2-treated SWNT suspension, implying that the oxidized Fermi level lies above the $n = 1$ state in the valence band in metallic tubes.

Rather, oxidative doping seems to affect the phonon structure and coupling to isoenergetic electronic states above the shifted Fermi level. A Fano line shape that depends sensitively on doping level has been observed in n-type degeneratively doped Si.[61] In Figure 17 we show the comparison of different TM Raman spectra from metallic tubes in thermally-treated, HNO_3-treated, and H_2SO_4/H_2O_2-treated bundles. Also shown is the Fano line shape fit to the broadened metallic Raman lines. The fitting parameters are listed in Table 2. From HNO_3-treated SWNTs to thermally-treated SWNTs, the normalized frequency ω_o is downshifted by ~12 cm^{-1}; the width Γ increases from 24 to 38 cm^{-1}. The Raman line shape gets more asymmetric, as reflected from the more negative asymmetry parameter $1/q$. These changes are similar to those observed in n-doped Si.[61]

In electrical transport measurements, gas exposure affects most significantly the carrier level and conductance of semiconducting nanotubes. However, in Raman measurement, this nanotube−adsorbates interaction is expected to affect mostly the Raman scattering from metallic nanotubes, because only metallic tubes have isoenergetic electronic states at the vibration energy ~1590 cm^{-1}. The excitation of the 1590 cm^{-1} phonon by isoenergetic fast electrons was evidenced in a recent high field electrical transport measurement on metallic SWNTs.[62] In our experiment, the large Raman line shape change on doping and degassing was observed with 632 nm excitation, which probes metallic nanotubes. We did not see the similar large change with 457 nm excitation, which mainly excites semiconducting nanotubes. Also the 632 nm RBM Raman scattering is found independent of oxidation by H_2SO_4/H_2O_2, consistent with theoretical predictions that long-range deformations (such as RBM phonon) do not couple to propagating electronic states in metallic tubes.[63,64] This model of nanotube−adsorbate interaction is also relevant to the resistivity difference between an

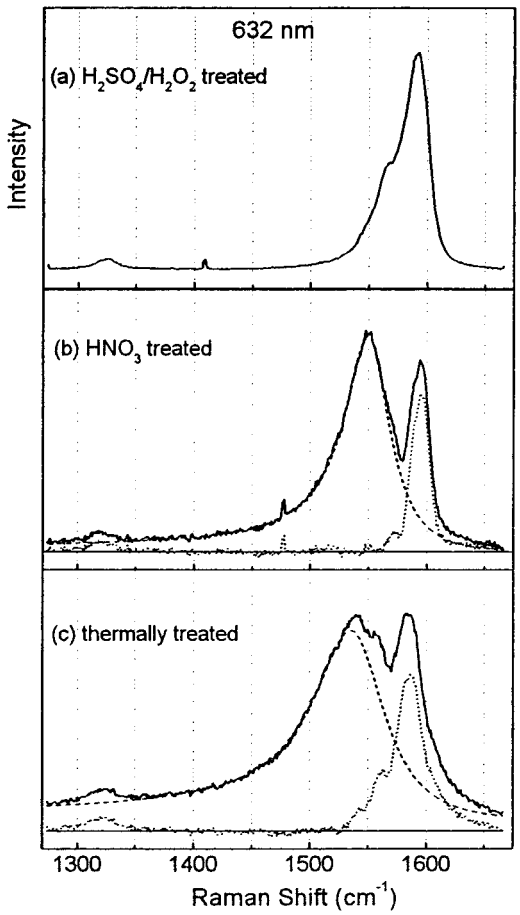

Figure 17. Comparison of tangential mode Raman spectra from metallic tubes in (a) H_2SO_4/H_2O_2-treated, (b) DMF-shortened (nitric acid treated), and (c) thermally- treated SWNT bundles. All the spectra were obtained using backscattering confocal Raman microscopy with 632 nm excitation. The dashed curves are Fano line shape fits to the broadened ~1550 cm^{-1} Raman line. The dotted curves are the remaining spectra after subtracting the Fano line fit from the experimental spectra.

TABLE 2: Fit Parameters for Fano Line Shape of Metallic Tangential Mode Raman Scattering

SWNTs	normalized frequency ω_o (cm^{-1})	line width Γ (cm^{-1})	asymmetry parameter $1/q$
HNO_3-treated	1552	24	−0.11
thermally-treated	1540	38	−0.13

acid-treated and a vacuum-annealed SWNT sample found by the Smalley group.[34] In their study, acid-treated sample showed metallic high conductivity, while after vacuum annealing it exhibited low conductivity. In the HNO_3-treated SWNT sample, we expect that charge transfer due to SWNT−doping molecule interaction oxidatively dopes nanotubes and makes ensemble sample more conductive. Once vacuum annealed, the sample is degassed and undoped, and shows higher resistivity.

We notice the large variation in tangential mode Raman scattering from metallic tubes (selected with 632 nm excitation) in the DMF-20 sample, while that from semiconducting SWNTs (with 457 nm excitation) remains the same for all the bundles studied, as shown in Figure 10. This suggests that the oxidative doping by nitric acid may not be uniform for all the bundles.

Conclusion

In summary, we have been able to measure Rayleigh scattering spectra and Raman spectra from individual bundles of aligned SWNTs, and to study the orientation dependence of Rayleigh scattering and Raman scattering properties of carbon nanotubes. The Rayleigh scattering spectrum exhibits resonance peaks due to the optically allowed interband transitions in SWNTs, which also appear in optical absorption spectrum of the bulk SWNT suspension. These resonance peaks were completely suppressed when the incident light polarization is perpendicular to the nanotube axis, suggesting that the optically allowed interband transition dipoles in SWNTs are orientated parallel to the tube axis. This is expected from group theory consideration and theoretical calculations. Polarized Raman measurements on aligned nanotubes in a bundle reveal that the Raman scattering signal is strongly polarized along the tube axis. Raman scattering intensity of both breathing mode and tangential mode decreases almost monotonically when the bundle is rotated away from the incident light polarization. It can be interpreted as resulting from the resonance effect due to the interband transition in SWNTs, whose dipoles are along the tube axis. The strong modes all behave as A_{1g}.

Tangential mode Raman spectrum from metallic nanotubes was found to show more variation from bundle to bundle than that from semiconducting tubes, which is consistent with the origin of the broadening metallic Raman peak. This broadened metallic Raman scattering at 1550 cm^{-1} can be well fitted by a BWF line shape function. We demonstrated that the metallic Raman scattering is sensitive to process conditions, thus suggesting that coupling of phonon to electronic states depends strongly on oxidative doping.

In agreement with previous work, we assign the broadened 1540 cm^{-1} Fano Raman peak in 632 nm Raman spectrum to the metallic tubes in the bundle. We suspect, but have not proven, that the sharp 1590 cm^{-1} peak in the 632 nm Raman spectrum most probably comes from semiconducting tubes in the same bundle.

Although we obtained a Raman spectrum from single SWNT bundles, it is still averaged over the different tubes in a bundle and the spectrum does not differ very much from ensemble measurements. To characterize SWNTs at single tube level with Raman scattering is still a challenging problem.

Acknowledgment. The authors thank Dr. Phaedon Avouris and Prof. Aron Pinczuk for stimulating discussions, Prof. Jie Liu (Duke University) and Dr. Hongbin Fang for the help in sample processing, Dr. Todd Krauss, Dr. Stan Wong, and Amy Michaels for the help in AFM and optical measurements. This work was supported by the DOE under Contract FG02-98ER14861. We have used materials characterization facilities at Columbia University supported by NSF MRSEC Grant DMR-98-09687. We thank the W. M. Keck foundation for a nanotechnology equipment grant.

References and Notes

(1) Iijima, S.; Ichihashi, T. *Nature* **1993**, *363*, 603.
(2) Bethune, D. S.; Chiang, C. H.; Vries, M. S. d.; Gorman, G.; Savoy, R.; Vazquez, J.; Beyers, R. *Nature* **1993**, *363*, 605.
(3) Dresselhaus, M. S.; Dresselhaus, G.; Eklund, P. C. *Science of Fullerenes and Carbon Nanotubes*; Academic Press: San Diego, 1996.
(4) Saito, R.; Dresselhaus, G.; Dresselhaus, M. S. *Physical Properties of Carbon Nanotubes*; Imperial College Press: London, 1998.
(5) Saito, R.; Fujita, M.; Dresselhaus, G.; Dresselhaus, M. S. *Appl. Phys. Lett.* **1992**, *60*, 2204.
(6) Tans, S. J.; Devoret, M. H.; Dai, H. J.; Thess, A.; Smalley, R. E.; Geerligs, L. J.; Dekker, C. *Nature* **1997**, *386*, 474.
(7) Bockrath, M.; Cobden, D. H.; McEuen, P. L.; Chopra, N. G.; Zettl, A.; Thess, A.; Smalley, R. E. *Science* **1997**, *275*, 1922.
(8) Tans, S. J.; Verschueren, A. R. M.; Dekker, C. *Nature* **1998**, *393*, 49.
(9) Yao, Z.; Postma, H. W. C.; Balents, L.; Dekker, C. *Nature* **1999**, *402*, 273.
(10) Dai, H. J.; Hafner, J. H.; Rinzler, A. G.; Colbert, D. T.; Smalley, R. E. *Nature* **1996**, *384*, 147.
(11) Dillon, A. C.; Jones, K. M.; Bekkedahl, T. A.; Kiang, C. H.; Bethune, D. S.; Heben, M. J. *Nature* **1997**, *386*, 377.
(12) Ye, Y.; Ahn, C. C.; Witham, C.; Fultz, B.; Liu, J.; Rinzler, A. G.; Colbert, D.; Smith, K. A.; Smalley, R. E. *Appl. Phys. Lett.* **1999**, *74*, 2307.
(13) Liu, C.; Fan, Y. Y.; Liu, M.; Cong, H. T.; Cheng, H. M.; Dresselhaus, M. S. *Science* **1999**, *286*, 1127.
(14) Saito, R.; Fujita, M.; Dresselhaus, G.; Dresselhaus, M. S. *Phys. Rev. B* **1992**, *46*, 1804.
(15) Wildoer, J. W. G.; Venema, L. C.; Rinzler, A. G.; Smalley, R. E.; Dekker, C. *Nature* **1998**, *391*, 59.
(16) Odom, T. W.; Huang, J.; Kim, P.; Lieber, C. M. *Nature* **1998**, *391*, 62.
(17) Odom, T. W.; Huang, J. L.; Kim, P.; Lieber, C. M. *J. Phys. Chem. B* **2000**, *104*, 2794.
(18) Rao, A. M.; Richter, E.; Bandow, S.; Chase, B.; Eklund, P. C.; Williams, K. A.; Fang, S.; Subbaswamy, K. R.; Menon, M.; Thess, A.; Smalley, R. E.; Dresselhaus, G.; Dresselhaus, M. S. *Science* **1997**, *275*, 187.
(19) Charlier, J. C.; Lambin, P. *Phys. Rev. B* **1998**, *57*, R15037.
(20) Kataura, H.; Kumazawa, Y.; Maniwa, Y.; Umezu, I.; Suzuki, S.; Ohtsuka, Y.; Achiba, Y. *Synth. Met.* **1999**, *103*, 2555.
(21) Brown, S. D. M.; Corio, P.; Marucci, A.; Dresselhaus, M. S.; Pimenta, M. A.; Kneipp, K. *Phys. Rev. B* **2000**, *61*, R5137.
(22) Chen, J.; Hamon, M. A.; Hu, H.; Chen, Y.; Rao, A. M.; Eklund, P. C.; Haddon, R. C. *Science* **1998**, *282*, 95.
(23) Jost, O.; Gorbunov, A. A.; Pompe, W.; Pichler, T.; Friedlein, R.; Knupfer, M.; Reibold, M.; Bauer, H. D.; Dunsch, L.; Golden, M. S.; Fink, J. *Appl. Phys. Lett.* **1999**, *75*, 2217.
(24) Knupfer, M.; Pichler, T.; Golden, M. S.; Fink, J.; Rinzler, A.; Smalley, R. E. *Carbon* **1999**, *37*, 733.
(25) Pimenta, M. A.; Marucci, A.; Brown, S. D. M.; Matthews, M. J.; Rao, A. M.; Eklund, P. C.; Smalley, R. E.; Dresselhaus, G.; Dresselhaus, M. S. *J. Mater. Res.* **1998**, *13*, 2396.
(26) Saito, R.; Takeya, T.; Kimura, T.; Dresselhaus, G.; Dresselhaus, M. S. *Phys. Rev. B* **1998**, *57*, 4145.
(27) Pimenta, M. A.; Marucci, A.; Empedocles, S. A.; Bawendi, M. G.; Hanlon, E. B.; Rao, A. M.; Eklund, P. C.; Smalley, R. E.; Dresselhaus, G.; Dresselhaus, M. S. *Phys. Rev. B* **1998**, *58*, R16016.
(28) Duesberg, G. S.; Blau, W. J.; Byrne, H. J.; Muster, J.; Burghard, M.; Roth, S. *Chem. Phys. Lett.* **1999**, *310*, 8.
(29) Kneipp, K.; Kneipp, H.; Corio, P.; Brown, S. D. M.; Shafer, K.; Motz, J.; Perelman, L. T.; Hanlon, E. B.; Marucci, A.; Dresselhaus, G.; Dresselhaus, M. S. *Phys. Rev. Lett.* **2000**, *84*, 3470.
(30) Corio, P.; Brown, S. D. M.; Marucci, A.; Pimenta, M. A.; Kneipp, K.; Dresselhaus, G.; Dresselhaus, M. S. *Phys. Rev. B* **2000**, *61*, 13202.
(31) Yu, Z.; Brus, L. *J. Phys. Chem. A* **2000**, *47*, 10995.
(32) Guo, T.; Nikolaev, P.; Thess, A.; Colbert, D. T.; Smalley, R. E. *Chem. Phys. Lett.* **1995**, *243*, 49.
(33) Thess, A.; Lee, R.; Nikolaev, P.; Dai, H. J.; Petit, P.; Robert, J.; Xu, C. H.; Lee, Y. H.; Kim, S. G.; Rinzler, A. G.; Colbert, D. T.; Scuseria, G. E.; Tomanek, D.; Fischer, J. E.; Smalley, R. E. *Science* **1996**, *273*, 483.
(34) Rinzler, A. G.; Liu, J.; Dai, H.; Nikolaev, P.; Huffman, C. B.; Rodriguez-Macias, F. J.; Boul, P. J.; Lu, A. H.; Heymann, D.; Colbert, D. T.; Lee, R. S.; Fischer, J. E.; Rao, A. M.; Eklund, P. C.; Smalley, R. E. *Appl. Phys. A* **1998**, *67*, 29.

(35) Liu, J.; Casavant, M. J.; Cox, M.; Walters, D. A.; Boul, P.; Lu, W.; Rimberg, A. J.; Smith, K. A.; Colbert, D. T.; Smalley, R. E. *Chem. Phys. Lett.* **1999**, *303*, 125.
(36) Burghard, M.; Duesberg, G.; Philipp, G.; Muster, J.; Roth, S. *Adv. Mater.* **1998**, *10*, 584.
(37) Muster, J.; Burghard, M.; Roth, S.; Duesberg, G. S.; Hernandez, E.; Rubio, A. *J. Vac. Sci. Technol. B* **1998**, *16*, 2796.
(38) Gerdes, S.; Ondarcuhu, T.; Cholet, S.; Joachim, C. *Europhys. Lett.* **1999**, *48*, 292.
(39) White, C. T.; Mintmire, J. W. *Nature* **1998**, *394*, 29.
(40) Burteaux, B.; Claye, A.; Smith, B. W.; Monthioux, M.; Luzzi, D. E.; Fischer, J. E. *Chem. Phys. Lett.* **1999**, *310*, 21.
(41) Ajiki, H.; Ando, T. *Jpn. J. Appl. Phys. Part 2-Lett.* **1994**, *34*, 107.
(42) Tang, Z. K.; Sun, H. D.; Wang, J.; Chen, J.; Li, G. *Appl. Phys. Lett.* **1998**, *73*, 2287.
(43) Rao, A. M.; Bandow, S.; Richter, E.; Eklund, P. C. *Thin Solid Films* **1998**, *331*, 141.
(44) Bandow, S.; Asaka, S.; Saito, Y.; Rao, A. M.; Grigorian, L.; Richter, E.; Eklund, P. C. *Phys. Rev. Lett.* **1998**, *80*, 3779.
(45) Venkateswaran, U. D.; Rao, A. M.; Richter, E.; Menon, M.; Rinzler, A.; Smalley, R. E.; Eklund, P. C. *Phys. Rev. B* **1999**, *59*, 10928.
(46) Alvarez, L.; Righi, A.; Guillard, T.; Rols, S.; Anglaret, E.; Laplaze, D.; Sauvajol, J. L. *Chem. Phys. Lett.* **2000**, *316*, 186.
(47) Milnera, M.; Kurti, J.; Hulman, M.; Kuzmany, H. *Phys. Rev. Lett.* **2000**, *84*, 1324.
(48) Rafailov, P. M.; Jantoljak, H.; Thomsen, C. *Phys. Rev. B* **2000**, *61*, 16179.
(49) Eklund, P. C.; Subbaswamy, K. R. *Phys. Rev. B* **1979**, *20*, 5157.
(50) Tuinstra, F.; Koenig, J. L. *J. Chem. Phys.* **1970**, *53*, 1126.
(51) Adams, G. B.; Sankey, O. F.; Page, J. B.; O'Keeffe, M.; Drabold, D. A. *Science* **1992**, *256*, 1792.
(52) Zhang, S.; Zhao, S.; Lu, J.; Xia, M. *Phys. Rev. B* **2000**, *61*, 12693.
(53) Rinzler, A. G.; Hafner, J. H.; Nikolaev, P.; Lou, L.; Kim, S. G.; Tomanek, D.; Nordlander, P.; Colbert, D. T.; Smalley, R. E. *Science* **1995**, *269*, 1550.
(54) Kong, J.; Franklin, N. R.; Zhou, C.; Chapline, M. G.; Peng, S.; Cho, K.; Dai, H. *Science* **2000**, *287*, 622.
(55) Sun, H. D.; Tang, Z. K.; Chen, J.; Li, G. *Solid State Commun.* **1999**, *109*, 365.
(56) Richter, E.; Subbaswamy, K. R. *Phys. Rev. Lett.* **1997**, *79*, 2738.
(57) Rao, A. M.; Jorio, A.; Pimenta, M. A.; Dantas, M. S. S.; Saito, R.; Dresselhaus, G.; Dresselhaus, M. S. *Phys. Rev. Lett.* **2000**, *84*, 1820.
(58) Rao, A. M.; Eklund, P. C.; Bandow, S.; Thess, A.; Smalley, R. E. *Nature* **1997**, *388*, 257.
(59) Petit, P.; Mathis, C.; Journet, C.; Bernier, P. *Chem. Phys. Lett.* **1999**, *305*, 370.
(60) Kazaoui, S.; Minami, N.; Jacquemin, R.; Kataura, H.; Achiba, Y. *Phys. Rev. B* **1999**, *60*, 13339.
(61) Abstreiter, G.; Cardona, M.; Pinczuk, A. Light Scattering by Free Carrier Excitations in Semiconductors. In *Light Scattering in Solids IV*; Cardona, M., Guntherodt, G., Eds.; Springer-Verlag: Berlin, Heidelberg, 1984.
(62) Yao, Z.; Kane, C. L.; Dekker, C. *Phys. Rev. Lett.* **2000**, *84*, 2941.
(63) Ando, T.; Nakanishi, T. *J. Phys. Soc. Jpn.* **1998**, *67*, 1704.
(64) McEune, P. L.; Bockrath, M.; Cobden, D. H.; Yoon, Y.-G.; Louie, S. G. *Phys. Rev. Lett.* **1999**, *83*, 5098.